



Comparison of electrical sensing and image analysis for *in situ* transmission electron microscopy nanomechanical testing of thin films

Sandra Stangebye^a, Xing Liu^b, Lina Daza Llanos^b, Yichen Yang^b, Ting Zhu^b, Josh Kacher^a, Olivier Pierron^{b,*}

^a School of Materials Science and Engineering, Georgia Institute of Technology, Atlanta, GA 30332, USA

^b Woodruff School of Mechanical Engineering, Georgia Institute of Technology, Atlanta, GA 30332, USA

ARTICLE INFO

Keywords:

In situ transmission electron microscopy

Nanomechanics

Activation volume

ABSTRACT

An *in situ* transmission electron microscopy (TEM) microelectromechanical system (MEMS) device has been designed to utilize TEM imaging for measuring stress and strain of thin film micro-specimens while simultaneously recording the microstructure evolution. Digital image correlation is also used to measure local normal strain values by tracking edge features of the specimens. The device performance is compared to that of a similar MEMS device that utilizes capacitive sensors for stress and strain measurements, using 100-nm thick Au thin film specimens. It is shown that there is a significant improvement in the noise levels from ~ 1 – 2 MPa to ~ 0.2 MPa and increased sensitivity with the capability of measuring small stress changes. The device can be used to perform both *in situ* TEM monotonic and transient tests (for activation volume measurements) to investigate the active plastic deformation mechanisms.

1. Introduction

Alternative deformation mechanisms are activated as grain size decreases into the ultrafine-grained (UFG) and nanocrystalline (NC) regimes of thin films [1–4]. This is accompanied by an increase in strength following the Hall-Petch law [5] due to grain boundaries (GBs) serving as obstacles to prolonged dislocation glide, along with participating directly in deformation through GB migration and GB sliding [6–11]. Since the active deformation mechanisms dictate the plastic kinetics, understanding these deformation mechanisms is key to designing metals with desired mechanical properties. To that end, quantitative characterization of the active deformation mechanisms is required. Atomistic simulations provide useful information regarding the plastic kinetics of individual mechanisms [12–15]; however, they suffer from time- and small-scale limitations that make comparing with experimental results nontrivial. The temporal and spatial resolution of transmission electron microscopy (TEM) provides an avenue to characterize both the microstructure and mechanical response when combined with *in situ* nanomechanical techniques [16].

There are a variety of nanomechanical platforms that have been utilized for *in situ* TEM straining experiments, each having their own advantages and disadvantages [16–21]. The key difference across

techniques is the way in which the force and displacement (strain) are measured. Push-to-pull (PTP) devices, commonly used to perform *in situ* TEM mechanical experiments, convert the compression motion of a nanoindenter into tensile forces on the specimen [20,22–24]. These devices require TEM nanoindenter holders that produce the raw force and displacement data and suffer from thermal drift of the indenter tip which limits the capability to perform transient experiments with timescales on the order of 30 s (see Section 2.4 for details). Other platforms utilize Micro Electro Mechanical Systems (MEMS) devices to electrically-control actuation and sensing [19,25–32]. These devices are typically composed of an actuator that provides a displacement (either through electrostatic forces or thermal expansion) and a sensor (beams of known bending stiffness) that measures the force on the specimen [33–37]. Pierron and co-workers have used two capacitive sensors to determine the displacements of the actuator and load sensor, which allows for the independent measurement of stress and strain [25]. This technique was employed to measure the monotonic stress-strain curves of thin film specimens as well as true activation volume, while performing TEM observations of the evolving microstructure [33–37]. However, this technique suffers from a low experimental yield that is related to challenges in measuring sub-femtofarad (fF) level signals without parasitic noise. Additional techniques integrate MEMS-based

* Corresponding author at: 801 Ferst Drive, Woodruff School of Mechanical Engineering, Atlanta, GA 30332-0405, USA.

E-mail address: olivier.pierron@me.gatech.edu (O. Pierron).

actuation while relying on conventional TEM imaging to measure the displacement of the force and displacement sensors [38,39]. The advantage of these techniques is that the displacement resolution is controlled by the resolution of the TEM and does not require calibration of the displacement sensors. However, these techniques do not allow for high-magnification recording of the microstructure during stress and strain measurement. Modern TEM detectors routinely have 16 megapixels or more, providing a means to digitally enlarge images post collection while retaining feature sharpness and obtain information related to microstructure evolution, such as grain growth and/or GB migration.

In this paper, we provide a MEMS design that utilizes TEM imaging to reliably measure stress and strain while simultaneously recording the microstructure evolution. We compare the performance with our capacitive sensing-based MEMS device and show that the noise and resolution is improved using the image-based technique. We also introduce a digital image correlation technique to measure local normal strain values along the specimen's gauge length, by tracking edge features.

2. Experimental details

2.1. Principles of operation of MEMS platforms

The MEMS devices used in this study are shown in Fig. 1. The MEMS device shown in Fig. 1(a) is referred to as the 'capacitive-sensing' device since it utilizes two capacitive sensors (CS_1 and CS_2) to measure the displacement of the thermal actuator (TA) and load sensor (LS) beam. This device has been used in Refs [25,26,33,34,36,37] to perform *in situ* TEM straining experiments. The device shown in Fig. 1(b) is the 'image-based' device. Instead of relying on capacitive sensors for displacement measurements, it utilizes TEM imaging to record the displacement of the actuator and load sensor beam directly. Both devices are composed of similar TAs and LS beams. The TAs are composed of ten inclined pairs of beams that provide the displacement when a voltage is applied across the beams (through resistive heating). A large heat sink is

provided between the thermal actuator and the specimen gap to limit the temperature increase of the specimen [32]. The main differences between the devices are that both the capacitive sensors have been removed and a stationary beam (SB) is located within the specimen gap. The SB is in between the two Si pads of the specimen gap (shown at a higher magnification in Fig. 1(c)). The oxide bridge (SiO_2 B) serves to physically connect the TA to the specimen gap while providing electrical isolation (which was previously done by using epoxy glue).

During operation, the shift in the central shuttle causes a shift in the specimen gap (specifically causes a shift in the Si pad labeled 'A' in Fig. 1(c)). Since this pad is rigidly connected to the TA, this shift is equal to the displacement of the actuator X_A . If a specimen is mounted on the device, a portion of this displacement is transmitted to the LS beam via the specimen. Since the Si pad 'B' is rigidly connected to the LS beam, the displacement of 'B' is equal to the displacement of the LS (X_{LS}). Measuring X_A and X_{LS} independently requires a stationary reference point, which is provided by the SB that is located in between specimen gap pad 'A' and 'B'. The schematic shown in Fig. 1(d) illustrates how the measurements are determined. At $V_{in} = 0$, there is no applied voltage and the initial distance between the SB and the top and bottom specimen pads are indicated by the brown arrows and labelled 1 and 2, respectively. After a voltage is applied ($V_{in} = V$), pad 'A' is shifted by X_A and pad 'B' and the load sensor by X_{LS} . Measuring these simultaneously requires a fixed object to be able to separate the total increase in the specimen gap into the two components (X_A and X_{LS}). To do this, the gap sizes indicated by the dashed brown arrows are compared to the original gap sizes (solid brown arrows labelled 1 and 2) to determine X_A and X_{LS} . An adequate TEM magnification is chosen to ensure that the gap 1 and gap 2 are both in view. The video and/or images taken are analysed in real-time using a Python code integrated into the TEM Gatan videoing software or processed post-mortem using MATLAB. In either case, the programs determine the size (distance) of Gap 1 and Gap 2 for every frame by identifying the edges of Gap 1 and Gap 2 to produce 4 lines (one for each edge). As the video/experiment progresses, the program records the locations and alignment of these lines. The tilt angle between the edges and the imaging window is appropriately considered in the calculation of gap sizes. The values of X_A and X_{LS} are thus determined by considering how much the gap sizes (distance between lines) change throughout the experiment with respect to the original gap size.

Both devices are wire bonded to a chip carrier designed for the 7-lead Hummingbird Scientific electrical biasing TEM holder. The experiments are performed in a ThermoFisher Tecnai F30 TEM operating at 300 kV.

2.2. Stress and strain measurements

Once the displacements of the actuator and load sensor are determined, the displacement of the specimen X_S can be calculated by $X_S = X_A - X_{LS}$. Similarly, the force can be calculated by considering the known stiffness K_{LS} of the load sensor beams following $F = K_{LS}X_{LS}$. Stress and strain are then calculated by considering the specimen geometry. The gauge length (l) is estimated by measuring the free-standing portion from SEM images taken before or after the experiment and the gauge width (w) is estimated prior to the experiment from TEM images. The specimen thickness (t) is pre-defined per the fabrication recipe. The (engineering) stress (σ) and strain (ϵ) are calculated following:

$$\sigma = \frac{F}{tw} \quad (1)$$

$$\epsilon = \frac{X_S}{l} \quad (2)$$

In most cases, the calculated stress values are modified slightly by pre-stress that is present [33]. The specimens are clamped onto the specimen gap using UV curable glue. The glue shrinks during curing which can lead to tensile forces on the specimen prior to the experiment. The pre-stress values typically range from 10 to 200 MPa and is

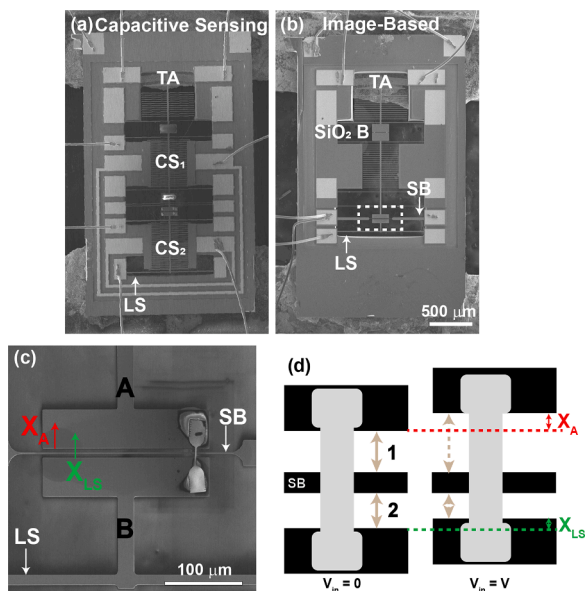


Fig. 1. SEM images of MEMS devices. (a) Capacitive-sensing MEMS with capacitive sensors (CS_1 and CS_2) labeled and (b) image-based MEMS devices. The thermal actuator (TA), and load sensor beams (LS) are common to both. The image-based MEMS contains an SiO_2 bridge (SiO_2 B) and stationary beam (SB). The specimen gap in (b) is outlined and shown in more detail in (c). The displacement of the actuator X_A and load sensor X_{LS} are indicated. (d) schematic of the image-based MEMS operation.

estimated by determining the distance the LS beam is deflected before and after curing of the glue. This can be done by comparing the ‘equilibrium’ distance between the SB and LS beam (prior to any specimen placement) and the initial gap prior to starting an experiment. The difference between these two distances is due to the pre-stress and is used to measure its value.

2.3. Local strain measurements

Our previous finite element modelling of the sample and glue (used for clamping) assembly highlighted inaccurate elastic strain measurements based on Eq. (2). The inaccuracy results from finite deformation in the fillet region of the specimens, as well as possible presence of glue underneath portion of the gauge section [26]. These finite deformations of the specimen outside of the gauge section result in calculated effective elastic moduli of Au samples to were 20 to 40% lower than the actual value. To obtain accurate elastic strain measurements, we employ a simple digital image correlation (DIC) technique that relies on tracking edge features of the specimens. The initial step in our methodology involves employing a cross-correlation algorithm to stabilize the video. This algorithm calculates the positional offset relative to the first image after binarization, offering a more consistent basis for image analysis. Subsequently, we perform cropping of the images to concentrate on the regions of interest. (i.e. the gauge section of the specimen). We then apply the Harris corner detection algorithm, a method for identifying corner features along the edges of the specimens. The Harris algorithm excels in detecting significant changes in all directions within an image segment and provides an added benefit of being resilient to contrast changes. Following that, we filter and normalize tracked centers that consistently appear across multiple frames. This careful filtration step such as setting threshold of maximum distance detected between two consecutive frames ensures only the most relevant data points are retained for strain computation. The strain is then computed using the $\Delta x/\text{Local Distance}$. Fig. 2 highlights the tracking of several features during a monotonic test to failure.

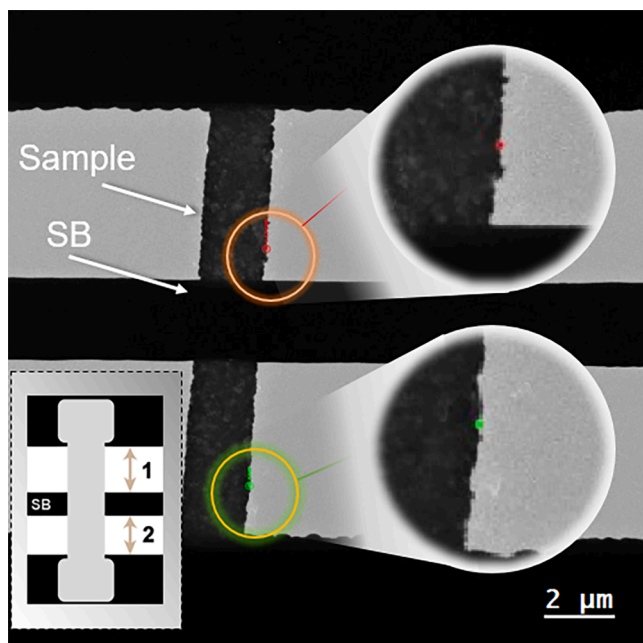


Fig. 2. – Post-test local strain measurement technique, relying on edge feature tracking. The TEM image (taken prior to the start of the test) shows two points along the sidewall of the specimen that were tracked throughout the duration of the test. The location of these two points during the test is also shown on this image.

2.4. Activation volume measurements

Both of the devices can be used to perform both monotonic tensile tests and transient tests such as repeated stress-relaxation experiments. This is useful as true activation volume, which is used to describe deformation mechanisms [15,33,34,40–43], can be measured by performing multiple stress-relaxation segments. With this technique, a stress-relaxation segment is performed by keeping the actuator displacement X_A constant (i.e. holding a constant V_m). This implies that during a relaxation:

$$X_A = X_S + X_{LS} = \text{constant} \quad (3)$$

As plastic deformation occurs during a relaxation segment, the plastic strain increases (X_S increases) which results in a decrease in X_{LS} and thus a measured decrease in stress. During a relaxation segment, the plastic strain rate can be determined following:

$$\dot{\epsilon}_p = -\dot{\sigma}/M \quad (4)$$

where $\dot{\sigma}$ is stress rate obtained by fitting the stress relaxation data with logarithmic fit and M is the machine-specimen stiffness [25,44]. The true activation volume V^* is defined using the following equation.

$$V^* = \sqrt{3}kT \frac{\ln(\dot{\epsilon}_{i2}/\dot{\epsilon}_{f1})}{\Delta\sigma_{12}} \quad (5)$$

In the above equation, $\dot{\epsilon}_{f1}$ and $\dot{\epsilon}_{i2}$ are the final and initial strain rates for the first and second relaxation segment, respectively and $\Delta\sigma_{12}$ is the stress increase during reloading (the $\sqrt{3}$ term is from converting the shear stress/strains to normal stress/strains following $\sigma = \sqrt{3}\tau$). Finally, V^* can be experimentally calculated by combining Eqn. (4) and (5) which yields:

$$V^* = \sqrt{3}kT \frac{\ln(\dot{\sigma}_{i2}/\dot{\sigma}_{f1})}{\Delta\sigma_{12}} \quad (6)$$

Using Eqn. (6) eliminates the dependency of V^* on the strain rate and instead implies that the accuracy of V^* depends on the stress rate, which is independent of gauge length and is more accurately determined using these MEMS devices.

2.5. Thin film specimen and MEMS fabrication

The specimens tested in this study are UFG Au films fabricated in a cleanroom using an optical lithography process and deposited using electron-beam evaporation to a final thickness of 100 nm. XeF_2 etch of the Si substrate reveals free-stranding microtensile specimens. The as-deposited films have an average grain size of 142 ± 68 nm. Some specimens were then annealed to 700°C for 5 min and have an average grain size of 768 ± 260 nm. The specimens are placed onto the MEMS devices (using micromanipulators under a light microscope) across the specimen gap and clamped using UV curable glue (shown in Fig. 1(b)).

The MEMS devices are fabricated with the SOIMUMPs process from MEMSCAP, using a $25\ \mu\text{m}$ -thick structural Si layer, and a $2\ \mu\text{m}$ -thick oxide layer. To ensure the specimen does not contact the stationary beam, a Focused Ion Beam (FIB) is used to mill away $2\text{--}3\ \mu\text{m}$ from the top of the stationary beam. Hence, the top surface of the stationary beam is $2\text{--}3\ \mu\text{m}$ below the top surface of the two Si pads onto which the specimen is glued, thereby preventing any contact between the specimen and the stationary beam.

3. Results and discussion

3.1. In situ TEM stress and strain measurements based on image analysis

An example of an *in situ* TEM monotonic experiment using the ‘image-based’ approach is shown in Fig. 3. The stress-strain curve is shown in Fig. 3(a). Snapshots taken from the continuous video recording

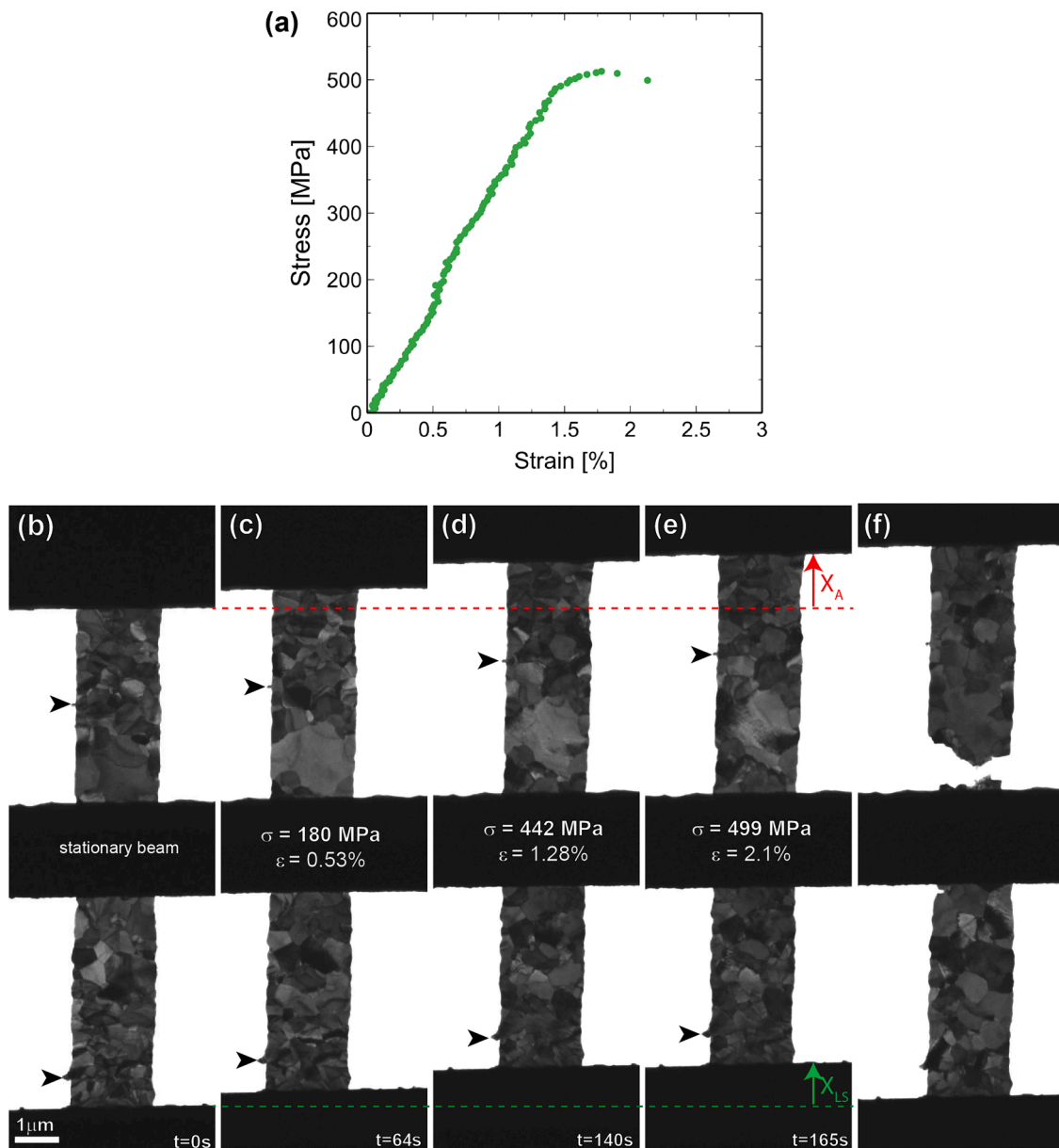


Fig. 3. *In situ* monotonic tensile test using the image-based MEMS technique. (a) stress-strain curve determined from X_A and X_{LS} , (b)–(d) TEM images captured throughout the experiment. The time stamp and far-field stress and strain levels are provided. (e) X_A and X_{LS} are indicated. (f) after specimen failure occurred.

during the experiments are shown in Fig. 3(b)–(f). In all of the frames, the stationary beam is visible to serve as the reference point. As a voltage is applied, the top Si pad is displaced by X_A and by being connected via the specimen, the bottom Si pad is displaced by X_{LS} . The progression of these displacements is easily visualized by noting the distance between the position of either pad and the red and green dotted line and labelled in Fig. 3(e).

3.2. Local strain measurements

Fig. 4(a) shows a comparison of the stress vs nominal strain and stress vs local strain (based on the procedure described in 2.3) for the test shown in Fig. 3 on an annealed Au specimen. In addition, Figs. 5(a)–(c) show the results of three tests on as-deposited Au specimens, also comparing nominal vs local strain. For each stress-strain curve, an elastic modulus value, E , is calculated based on a linear fit for stress values up to 250 MPa. For the four tests, the E values obtained using nominal strain (which is an effective E value, based on finite

compliances of the fillet region and of portions of the gauge section that are also glued [26]), are 46 to 66 % lower than the E values calculated based on local strain measurements (which range from 75 to 100 GPa for the four tests). The average E value (based on local strain measurements) is 86 GPa, and is consistent with bulk values of Au (80 GPa) that is expected for a $\langle 111 \rangle$ out-of-plane texture [33]. The measured effective E values are also consistent with prior FEM work that predicted a decrease compared to 80 GPa ranging from 16 to 42 %. The FEM work assumed an elastic modulus value of the epoxy glue of 3 GPa. A lower value for the actual epoxy used in the experiments could easily explain why our measurements show larger discrepancies between nominal and local strain values.

These results show that the local strain measurement technique enables accurate elastic strain measurements that were not possible with the capacitive sensing technique. Fig. 4(b) and Figs. 5(d)–(f) show the corresponding stress vs plastic strain (calculated as the total strain minus the elastic strain (stress divided by E)) for both nominal and local strain values. In all cases, there is a good match between the nominal and local

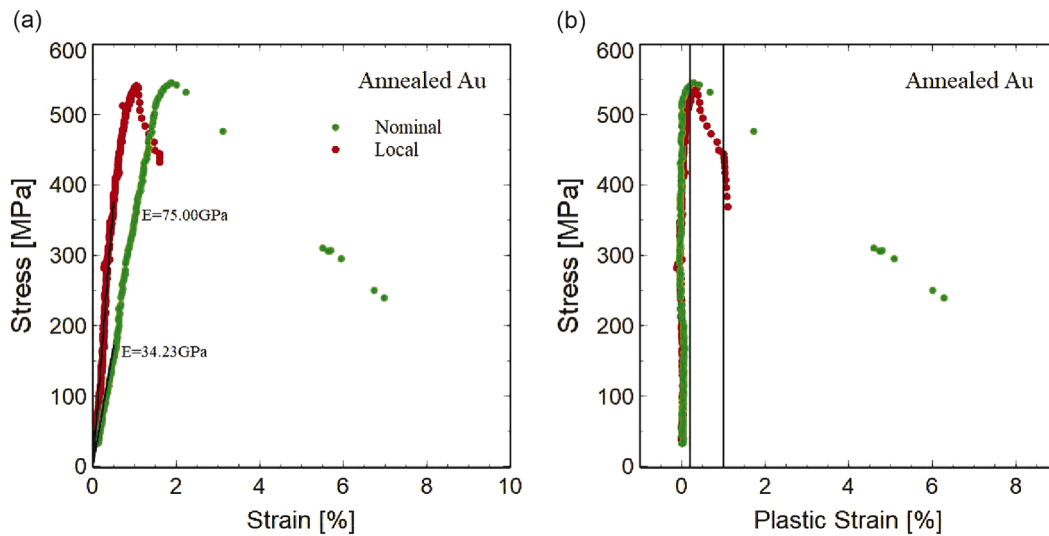


Fig. 4. (a) Comparison of the stress vs nominal strain and stress vs local strain curves for an annealed Au monotonic test (also shown in Fig. 3) (b) Corresponding stress vs plastic strain curves.

curves up to the onset of necking (defining the ultimate tensile strength). Past necking, the discrepancy between the curves results from the actual locations of strain localization (within or outside the tracked points used for local strain measurements). The vertical lines at a plastic strain of 0.2 % and 1 % can be used to measure yield strengths corresponding to these plastic strain values.

3.3. Comparing with capacitive sensing technique

The performance of the capacitive sensing and image analysis were compared using the following approach. A test was performed with a capacitive sensing MEMS while simultaneously using the TEM to video CS_2 throughout the experiment (CS_2 is connected to the LS beam so the displacement of CS_2 is equal to the deflection of the LS beam). This allows for the comparison of X_{LS} determined from capacitive sensing measurements with the X_{LS} determined manually from the CS_2 video (similar to how X_{LS} is measured in the image-based MEMS). The result of a monotonic experiment is shown in Fig. 6 with the overlaid data from both methods for measuring stress. This shows a reasonable match between the image-based and capacitive sensing-based data. The match indicates that the electrical sensing calibration procedure [26,33], which is performed prior to any test to calibrate the capacitive readout sensor, works. However, there appears to be minor variations (up to 50 MPa in stress) after specimen yielding occurs and during specimen failure, which likely indicates that the assumption of a constant calibration factor during is test is not strictly valid. Hence, the image analysis, which does not rely on any calibration (pixel size is known), provides more accurate results. In addition, the noise in the image-based data is less than the electrical sensing-based (including fewer outliers), which is another advantage of this sensing technique.

Comparing the performance during transient experiments is important since stress-relaxation experiments can be used to characterize rate-governing deformation mechanisms via activation volume measurements. Similar to Fig. 6, this is done by using the capacitive sensing MEMS while videoing CS_2 with the TEM throughout the experiment. However, now the loading is paused by holding a constant voltage V_{in} . The specimen deforms via time-dependant plastic deformation which leads to stress-relaxation (stress decrease) during the paused relaxation segment. Fig. 7(a) is the full stress vs. time curve for the experiment with both the data from capacitive sensing (black) and image-based (orange). At the beginning of the experiment, the image-based and capacitive sensing match up well in terms of the magnitude of the far-field stress levels. However, after 400-seconds the data begins to deviate with the

image-based results reaching slightly higher stress levels, which is similar to what is observed in Fig. 6. Fig. 7(b) is the X_{LS} vs. time data for the same experiment.

During this experiment, eight relaxation segments were performed prior to specimen failure (the specimen fails during the eighth segment). The first three segments occurred at stress levels of 174–183 MPa. At this (low) stress level, there is limited plastic deformation occurring and thus only a small amount of stress relaxation ($|\Delta\sigma|$). This can be seen in Fig. 8 (a) which shows the data from the 3rd relaxation segment. The image-based data (orange) shows minimal stress-relaxation with only $|\Delta\sigma| \sim 1$ MPa (corresponding to a 3-nm decrease in X_{LS}). Conversely, the large noise in the capacitive sensing data (black) yields inconclusive results. This indicates that the image-based technique has an increased sensitivity and is capable of detecting smaller changes in stress levels.

After the 3rd relaxation segment, the stress is increased to a higher level and multiple relaxations are performed again at $\sigma \sim 310$ –340 MPa (relaxations 4–6 in Fig. 7(a)). The larger stress level promotes plastic deformation which increases the stress-relaxation $|\Delta\sigma|$. This can be seen for relaxation segments #4, #6, and #7 in Fig. 8(b)–(d). In all cases, the amount of stress-relaxation increases as the relaxations progress. The image-based data achieve slightly larger relaxation levels which could once again be contributed to errors in the capacitive sensing calibration constant for the capacitive sensing data. Each dataset is fitted with a logarithmic fit (solid lines) which is necessary to measure V^* following Eqn. (6). The R^2 values for each fit can be used to estimate the signal-to-noise ratio (SNR). Previous work has shown that a $SNR > 5$ requires logarithmic fits with $R^2 > 0.9$, which is used as a criterion for accurate V^* measurements [33]. For all of the relaxations in this experiment, the R^2 values are larger for the image-based data than for the capacitive sensing, revealing that the capacitive MEMS suffers from increased noise levels. The decreased noise levels in the image-based technique indicates increased throughput of V^* measurements since $R^2 > 0.9$ is the chosen criterion. For example, all of these relaxation segments (#4–8) achieved $R^2 > 0.9$ using the image-based data, whereas only two relaxations met this criterion for the capacitive sensing data. The calculated apparent (V_a) and true (V^*) activation volume values for Relax #4, #5 and #6 are shown in Table 1. There is a larger spread in the V^* values from the capacitive sensing which is likely attributed to the high noise levels (low R^2).

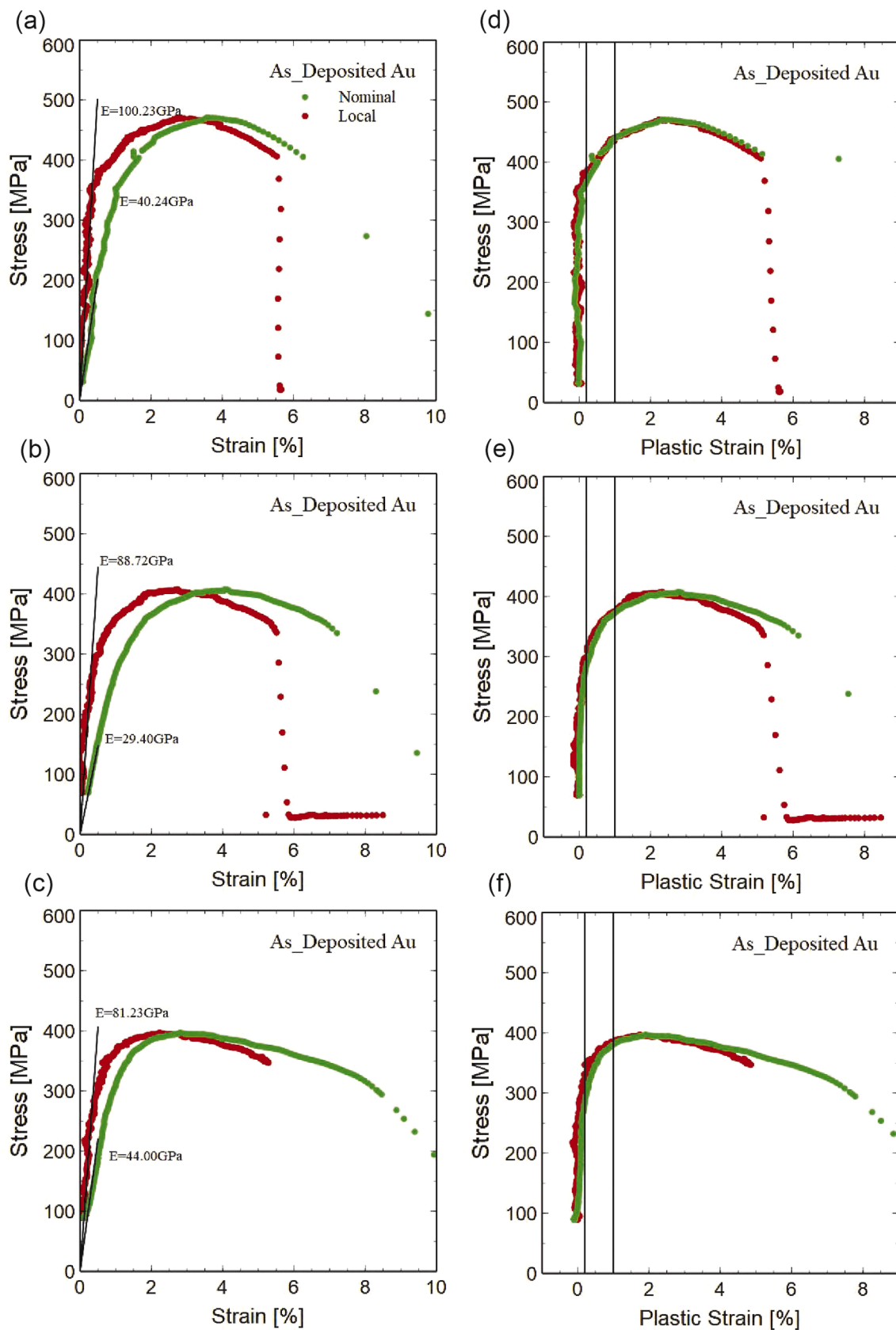


Fig. 5. (a)-(c) Comparison of the stress vs nominal strain and stress vs local strain curves for three as-deposited Au monotonic tests (d)-(f) Corresponding stress vs plastic strain curves.

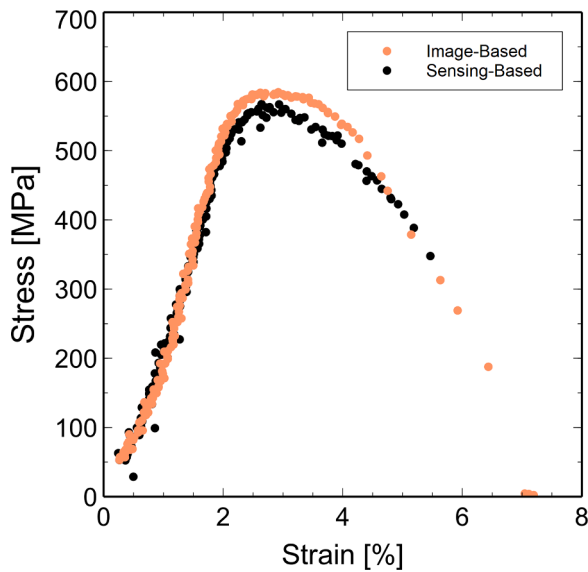


Fig. 6. Comparing electrical- and image-based sensing results under monotonic loading conditions for an UFG Au specimen.

3.4. Discussion

These results demonstrate that there is an improvement in the quality and throughput of successful tests by implementing the image-based approach to determine stress and strain during an *in situ* TEM straining experiment. While the capacitive sensing-based MEMS is a useful tool for characterizing the microstructure simultaneous to quantifying the mechanical properties [25,26,33,36], it suffers from a low experimental yield, mainly due to parasitic noise and long-term drift that can prevent accurate measurements of the sub fF-level capacitance signals. Comparing both techniques (Fig. 6 and Fig. 8) demonstrates that the image-based approach significantly improves the precision by reducing the noise levels. The capacitive sensing has a typical noise level of 0.1–0.2 fF in capacitance which translates to ~ 1 –2 MPa in stress [33] (based on the stiffness of the load sensor beams, K_{LS} , and the cross-section area of the specimens; see Eq.(1)). The image-based sensing has noise levels of ~ 0.2 nm, measured as the standard

deviation of the change in gap during a video under no applied voltage. This noise level corresponds to noise levels of ~ 0.2 MPa, also based on K_{LS} and the cross-section area of the specimens. Similarly, the image-based approach offers increased accuracy in the displacement measurements, which also implies it is capable of measuring small stress changes. This is very useful when studying materials that are less strain-rate sensitive than the current thin films, such as irradiated films that have limited plastic deformation/stress-relaxation [35].

Although measuring displacements using TEM imaging for stress/strain calculation has been previously demonstrated [38], the present MEMS device offers some advantages. The SB is positioned at the same location as the specimen itself which limits the required movement of the TEM stage as well as minimizes the magnification required to image the full specimen gap. This ensures that the magnification remains high enough to observe some microstructural details while simultaneously recording the required displacements. If higher magnification is desired for detailed analysis, the magnification can be adjusted to alternate between low enough to image the full specimen gap and high enough to image the desired features such as individual GBs and dislocations. There are also potential capabilities of the image-based MEMS that will be explored in the future. For example, running a current through the SB could locally increase the temperature of the specimen and facilitate conducting mechanical tests at elevated temperatures. This would provide a means to experimentally estimate activation energy and probe the temperature dependence of V^* [41], both of which would help elucidate the rate-controlling deformation mechanisms.

4. Conclusions

In situ TEM straining experiments were conducted using a MEMS device that utilizes the TEM to record and measure the displacements required to determine the stress and strain of the specimen. This is accomplished by designing the device with a stationary beam to serve as the necessary reference point. This device is capable of conducting both monotonic and stress-relaxation experiments. The performance is compared to that of a similar MEMS device that utilizes capacitive sensors to measure the displacement of the actuator and load sensor. It is shown that implementing the image-based approach provides a significant improvement in the noise levels and precision of the measurements. As such, the image-based MEMS is a promising technique for characterizing the plastic deformation mechanisms of thin films.

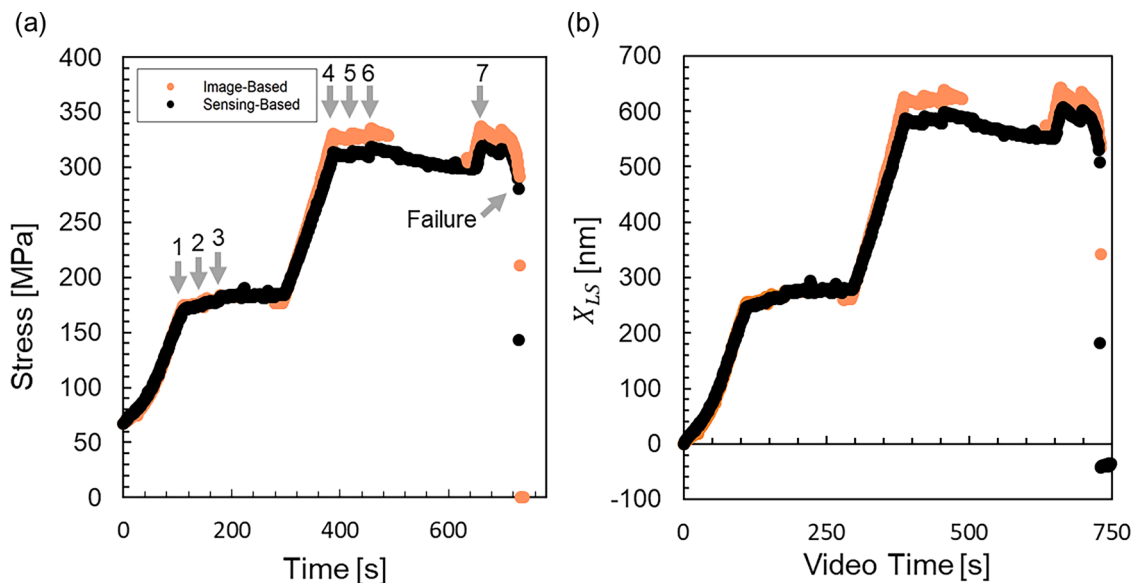


Fig. 7. Comparing capacitive sensing and image-based results during stress-relaxation experiment on UFG Au thin film. (a) Stress vs. time and X_{LS} vs. time (b) data for a full experiment until specimen failure. The seven relaxation segments are labeled in (a).

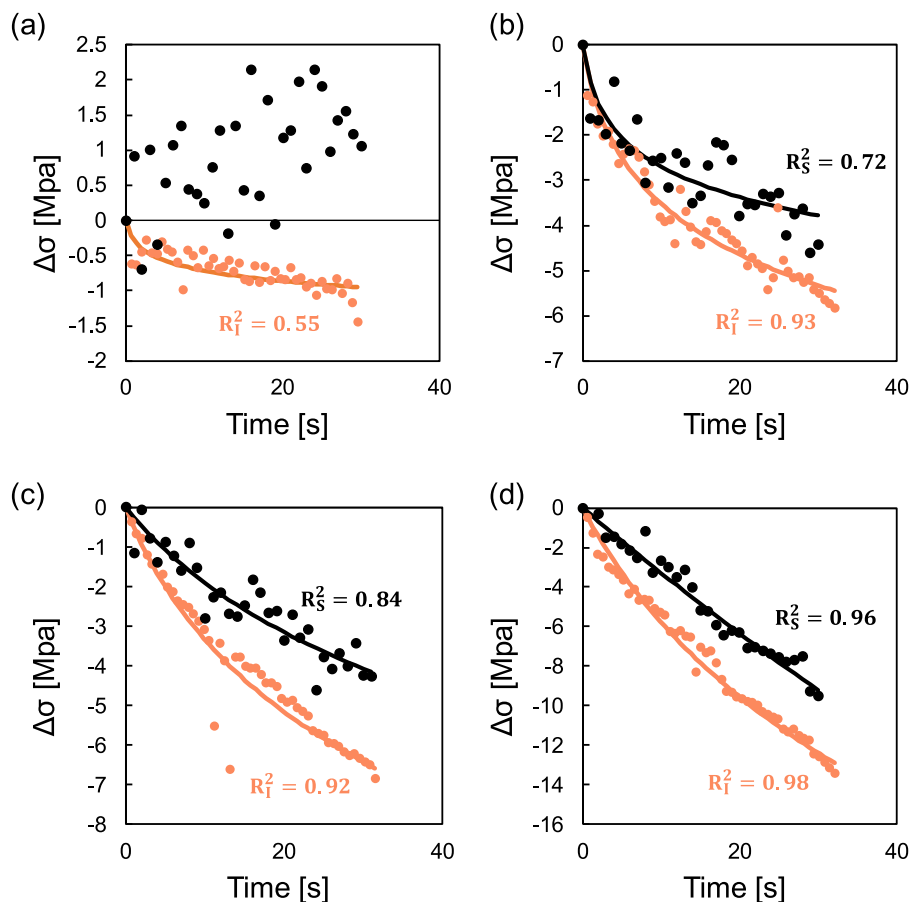


Fig. 8. Comparing capacitive sensing and image-based results during individual stress-relaxation segments for the experiment shown in Fig. 7. (a) Relaxation #3, (b) #4, (c) #6 and (d) #7. The solid lines are logarithmic fits of the corresponding datasets and the R^2 values for each fit is given.

Table 1

Comparing the calculated Apparent V_a , True Activation Volume V^* and R^2 values for image-based and capacitive sensing measurements for Relaxation #4, #5 and #6.

Relax #	Image-based			Capacitive Sensing		
	V_a (b^3)	V^* (b^3)	R^2	V_a (b^3)	V^* (b^3)	R^2
4	166	91	0.93	291	117	0.72
5	190	93	0.95	84	45	0.69
6	73	93	0.92	83	45	0.84

CRediT authorship contribution statement

Sandra Stangebye: Investigation, Writing – original draft. **Xing Liu:** Software. **Lina Daza Llanos:** Investigation. **Yichen Yang:** Software, Investigation. **Ting Zhu:** Supervision. **Josh Kacher:** Supervision. **Olivier Pierron:** Conceptualization, Writing – review & editing.

Declaration of Competing Interest

The authors declare that they have no known competing financial interests or personal relationships that could have appeared to influence the work reported in this paper.

Data availability

Data will be made available on request.

Acknowledgements

T.Z., J.K., and O.P. gratefully acknowledge support by the U.S. Department of Energy (DOE), Office of Science, Basic Energy Sciences (BES) Materials Science and Engineering (MSE) Division under Award #DE-SC0018960. S.S. is also supported by the U.S. Department of Energy (DOE) National Nuclear Security Administration (NNSA) Stewardship Science Graduate Fellowship (SSGF) program, provided under cooperative agreement number DE-NA0003960.

References

- [1] H. Van Swygenhoven, Footprints of plastic deformation in nanocrystalline metals, *Mater. Sci. Eng. A* 483–484 (2008) 33–39, <https://doi.org/10.1016/j.msea.2006.10.204>.
- [2] K.S. Kumar, H. Van Swygenhoven, S. Suresh, Mechanical behavior of nanocrystalline metals and alloys, *Acta Mater.* 51 (2003) 5743–5774, <https://doi.org/10.1016/j.actamat.2003.08.032>.
- [3] H. Van Swygenhoven, M. Spaczer, A. Caro, D. Farkas, Competing plastic deformation mechanisms in nanophase metals, *Phys. Rev. B* 60 (1999) 22–25, <https://doi.org/10.1103/PhysRevB.60.22>.
- [4] M.A. Meyers, A. Mishra, D.J. Benson, Mechanical properties of nanocrystalline materials, *Prog. Mater. Sci.* 51 (2006) 427–556, <https://doi.org/10.1016/j.pmatsci.2005.08.003>.
- [5] E.O. Hall, The deformation and ageing of mild steel: II characteristics of the Lüders deformation, *Proc. Phys. Soc. Section B* 64 (1951) 747–753, <https://doi.org/10.1088/0370-1301/64/9/302>.
- [6] T.J. Rupert, D.S. Gianola, Y. Gan, K.J. Hemker, Experimental observations of stress-driven grain boundary migration, *Science* (1979) 326 (2009) 1686–1690, <https://doi.org/10.1126/science.1178226>.
- [7] D.S. Gianola, D.H. Warner, J.F. Molinari, K.J. Hemker, Increased strain rate sensitivity due to stress-coupled grain growth in nanocrystalline Al, *Scr. Mater.* 55 (2006) 649–652, <https://doi.org/10.1016/j.scriptamat.2006.06.002>.
- [8] D.S. Gianola, S. Van Petegem, M. Legros, S. Brandstetter, H. Van Swygenhoven, K. J. Hemker, Stress-assisted discontinuous grain growth and its effect on the

- deformation behavior of nanocrystalline aluminum thin films, *Acta Mater.* 54 (2006) 2253–2263, <https://doi.org/10.1016/j.actamat.2006.01.023>.
- [9] M. Legros, D.S. Gianola, K.J. Hemker, *In situ* TEM observations of fast grain-boundary motion in stressed nanocrystalline aluminum films, *Acta Mater.* 56 (2008) 3380–3393, <https://doi.org/10.1016/j.actamat.2008.03.032>.
- [10] F. Momprou, D. Caillard, M. Legros, Grain boundary shear-migration coupling-I. *In situ* TEM straining experiments in Al polycrystals, *Acta Mater.* 57 (2009) 2198–2209, <https://doi.org/10.1016/j.actamat.2009.01.014>.
- [11] R. Gautier, A. Rajabzadeh, M. Larranaga, N. Combe, F. Momprou, M. Legros, Shear-coupled migration of grain boundaries: the key missing link in the mechanical behavior of small-grained metals? *Plast. Solid State Phys.* (2021) 1–16, <https://doi.org/10.5802/crphys.52>.
- [12] Y. Zhang, K. Ding, S. Stangebye, D. Chen, J. Kacher, O. Pierron, T. Zhu, Atomistic modeling of surface and grain boundary dislocation nucleation in FCC metals, *Acta Mater.* 237 (2022), 118155, <https://doi.org/10.1016/j.actamat.2022.118155>.
- [13] T. Zhu, J. Li, A. Samanta, A. Leach, K. Gall, Temperature and strain-rate dependence of surface dislocation nucleation, *Phys. Rev. Lett.* 100 (2008), 025502, <https://doi.org/10.1103/PhysRevLett.100.025502>.
- [14] T. Zhu, J. Li, S. Yip, Atomistic reaction pathway sampling: the nudge elastic band method and nanomechanics applications, *Nano Cell Mech.: Fundam. Front.* (2013) 313–338.
- [15] R.J. Asaro, S. Suresh, Mechanistic models for the activation volume and rate sensitivity in metals with nanocrystalline grains and nano-scale twins, *Acta Mater.* 53 (2005) 3369–3382, <https://doi.org/10.1016/j.actamat.2005.03.047>.
- [16] H.D. Espinosa, R.A. Bernal, T. Filleter, *in situ* TEM electromechanical testing of nanowires and nanotubes, *Small* 8 (2012) 3233–3252, <https://doi.org/10.1002/SMLL.201200342>.
- [17] M. Legros, *In situ* mechanical TEM: seeing and measuring under stress with electrons, *C R Phys.* 15 (2014) 224–240, <https://doi.org/10.1016/j.crrhy.2014.02.002>.
- [18] S. Bhowmick, H. Espinosa, K. Jungjohann, T. Pardoen, O. Pierron, Advanced microelectromechanical systems-based nanomechanical testing: beyond stress and strain measurements, *MRS Bull.* 44 (2019) 487–493, <https://doi.org/10.1557/mrs.2019.123>.
- [19] M.A. Haque, M.T.A. Saif, A Review of MEMS-Based Microscale and Tensile and Bending Testing Nanoscale, *Exp Mech.* 43 (2003) 248–255, <https://doi.org/10.1007/BF02410523>.
- [20] D.C. Bufford, D. Stauffer, W.M. Mook, S.A. Syed Asif, B.L. Boyce, K. Hattar, High cycle fatigue in the transmission electron microscope, *Nano Lett.* 16 (2016) 4946–4953, https://doi.org/10.1021/ACS.NANOLETT.6B01560/SUPPL_FILE/NL6B01560_SI_003.MOV.
- [21] G. Dehm, B.N. Jaya, R. Raghavan, C. Kirchlechner, Overview on micro- and nanomechanical testing: new insights in interface plasticity and fracture at small length scales, *Acta Mater.* 142 (2017) 248–282, <https://doi.org/10.1016/j.actamat.2017.06.019>.
- [22] A. Kobler, A. Kashiwar, H. Hahn, C. Kübel, Combination of *in situ* straining and ACOM TEM: a novel method for analysis of plastic deformation of nanocrystalline metals, *Ultramicroscopy* 128 (2013) 68–81, <https://doi.org/10.1016/j.ultramicro.2012.12.019>.
- [23] J.P. Liebig, M. Macković, E. Spiecker, M. Göken, B. Merle, Grain boundary mediated plasticity: a blessing for the ductility of metallic thin films? *Acta Mater.* 215 (2021), 117079 <https://doi.org/10.1016/j.actamat.2021.117079>.
- [24] S.H. Li, W.Z. Han, Z.W. Shan, Deformation of small-volume Al-4Cu alloy under electron beam irradiation, *Acta Mater.* 141 (2017) 183–192, <https://doi.org/10.1016/j.actamat.2017.09.015>.
- [25] S. Gupta, O.N. Pierron, MEMS based nanomechanical testing method with independent electronic sensing of stress and strain, *Extreme Mech. Lett.* 8 (2016) 167–176, <https://doi.org/10.1016/j.eml.2016.01.005>.
- [26] S. Gupta, O.N. Pierron, A MEMS tensile testing technique for measuring true activation volume and effective stress in nanocrystalline ultrathin microbeams, *Microelectromech. Syst.* 26 (2017) 1082–1092, <https://doi.org/10.1109/JMEMS.2017.2708522>.
- [27] R. Agrawal, H.D. Espinosa, Multiscale experiments: state of the art and remaining challenges, *J. Eng. Mater. Technol.* 131 (2009), <https://doi.org/10.1115/1.3183782>.
- [28] M.F. Pantano, R.A. Bernal, L. Pagnotta, H.D. Espinosa, Multiphysics design and implementation of a microsystem for displacement-controlled tensile testing of nanomaterials, *Meccanica* 50 (2015) 549–560, <https://doi.org/10.1007/s11012-014-9950-9>.
- [29] R. Ramachandramoorthy, M. Milan, Z. Lin, S. Trolrier-Mckinstry, A. Corigliano, H. Espinosa, Design of piezoMEMS for high strain rate nanomechanical experiments, *Extreme Mech. Lett.* 20 (2018) 14–20, <https://doi.org/10.1016/j.eml.2017.12.006>.
- [30] R. Ramachandramoorthy, W. Gao, R. Bernal, D. Horacio, High Strain rate tensile testing of silver nanowires: rate-dependent brittle-to-ductile transition, *Nano Lett.* 16 (2016) 255–263, <https://doi.org/10.1021/acs.nanolett.5b03630>.
- [31] Y. Zhu, T.-H. Chang, A review of microelectromechanical systems for nanoscale mechanical characterization, *J. Micromech. Microeng.* 25 (2015), 093001, <https://doi.org/10.1088/0960-1317/25/9/093001>.
- [32] B. Pant, S. Choi, E.K. Baumert, B.L. Allen, S. Graham, K. Gall, O.N. Pierron, MEMS-Based Nanomechanics: influence of MEMS Design on Test Temperature, *Exp. Mech.* 52 (2012) 607–617, <https://doi.org/10.1007/s11340-011-9526-8>.
- [33] S. Gupta, S. Stangebye, K. Jungjohann, B. Boyce, T. Zhu, J. Kacher, O.N. Pierron, *In situ* TEM measurement of activation volume in ultrafine grained gold, *Nanoscale* 12 (2020) 7146–7158, <https://doi.org/10.1039/d0nr01874k>.
- [34] S. Gupta, S. Stangebye, K. Jungjohann, B. Boyce, T. Zhu, J. Kacher, O.N. Pierron, Correction: *in situ* TEM measurement of activation volume in ultrafine grained gold, *Nanoscale* 13 (2021) 9040, <https://doi.org/10.1039/d1nr90099d>.
- [35] S. Stangebye, K. Ding, Y. Zhang, E. Lang, K. Hattar, T. Zhu, J. Kacher, O. Pierron, Direct Observation of Grain-Boundary-Migration-Assisted Radiation Damage Healing in Ultrafine Grained Gold under Mechanical Stress, *Nano Lett.* 23 (2023) 3282, https://doi.org/10.1021/ACS.NANOLETT.3C00180/SUPPL_FILE/NL3C00180_SI_009.AVI.
- [36] S. Stangebye, Y. Zhang, S. Gupta, E. Hosseinian, F. Yu, C. Barr, K. Hattar, O. N. Pierron, T. Zhu, J. Kacher, Grain growth of nanocrystalline aluminum under tensile deformation: a combined *in situ* TEM and atomistic study, *Mater.* (Oxf) 16 (2021), 101068, <https://doi.org/10.1016/j.mtla.2021.101068>.
- [37] S. Stangebye, Y. Zhang, S. Gupta, T. Zhu, O. Pierron, J. Kacher, Understanding and quantifying electron beam effects during *in situ* TEM nanomechanical tensile testing on metal thin films, *Acta Mater.* 222 (2022), 117441, <https://doi.org/10.1016/j.actamat.2021.117441>.
- [38] M.A. Haque, M.T.A. Saif, *In situ* tensile testing of nanoscale freestanding thin films inside a transmission electron microscope, *J. Mater. Res.* 20 (2005) 1769–1777, <https://doi.org/10.1557/JMR.2005.0220/METRICS>.
- [39] M.A. Haque, M.T.A. Saif, Deformation mechanisms in free-standing nanoscale thin films: a quantitative *in situ* transmission electron microscope study, *Proc. Natl. Acad. Sci. U S A* 101 (2004) 6335–6340, <https://doi.org/10.1073/PNAS.0400066101>.
- [40] Q. Wei, S. Cheng, K.T. Ramesh, E. Ma, Effect of nanocrystalline and ultrafine grain sizes on the strain rate sensitivity and activation volume: fcc versus bcc metals, *Mater. Sci. Eng.: A* 381 (2004) 71–79, <https://doi.org/10.1016/j.msea.2004.03.064>.
- [41] Y.M. Wang, A.V. Hamza, E. Ma, Temperature-dependent strain rate sensitivity and activation volume of nanocrystalline Ni, *Acta Mater.* 54 (2006) 2715–2726, <https://doi.org/10.1016/j.actamat.2006.02.013>.
- [42] Y.M. Wang, A.V. Hamza, E. Ma, Activation volume and density of mobile dislocations in plastically deforming nanocrystalline Ni, *Appl. Phys. Lett.* 86 (2005), <https://doi.org/10.1063/1.1946899>.
- [43] C. Duhamel, Y. Brechet, Y. Champion, Activation volume and deviation from Cottrell-Stokes law at small grain size, *Int. J. Plast.* 26 (2010) 747–757, <https://doi.org/10.1016/j.ijplas.2009.10.003>.
- [44] E. Hosseinian, M. Legros, O.N. Pierron, Quantifying and observing viscoplasticity at the nanoscale: highly localized deformation mechanisms in ultrathin nanocrystalline gold films, *Nanoscale* 8 (2016) 9234–9244, <https://doi.org/10.1039/c6nr00710d>.